Vortices in spin-orbit-coupled Bose-Einstein condensates

J. Radić,[1] T. A. Sedrakyan,[1] I. B. Spielman,[1,2] and V. Galitski[1]
[1]*Joint Quantum Institute, University of Maryland, College Park, Maryland 20742-4111, USA*
[2]*National Institute of Standards and Technology, Gaithersburg, Maryland 20899, USA*
(Received 24 August 2011; published 5 December 2011)

Realistic methods to create vortices in spin-orbit-coupled Bose-Einstein condensates are discussed. It is shown that, contrary to common intuition, rotation of the trap containing a spin-orbit condensate does not lead to an equilibrium state with static vortex structures but gives rise instead to nonequilibrium behavior described by an intrinsically time-dependent Hamiltonian. We propose here the following alternative methods to induce thermodynamically stable static vortex configurations: (i) to rotate both the lasers and the anisotropic trap and (ii) to impose a synthetic Abelian field on top of synthetic spin-orbit interactions. Effective Hamiltonians for spin-orbit condensates under such perturbations are derived for most currently known realistic laser schemes that induce synthetic spin-orbit couplings. The Gross-Pitaevskii equation is solved for several experimentally relevant regimes. The new interesting effects include spatial separation of left- and right-moving spin-orbit condensates, the appearance of unusual vortex arrangements, and parity effects in vortex nucleation where the topological excitations are predicted to appear in pairs. All these phenomena are shown to be highly nonuniversal and depend strongly on a specific laser scheme and system parameters.

DOI: 10.1103/PhysRevA.84.063604 PACS number(s): 03.75.Lm, 03.75.Mn, 85.75.−d

I. INTRODUCTION

Spin-orbit-coupled cold atoms represent a very new and quickly growing area of research that promises to host an even richer variety of exotic phenomena than solid-state spintronics [1]. Indeed, within just a few years of experimental research in the field, a number of exciting phenomena have already been observed [2–5] and there are clearly many more low-lying fruits awaiting their experimental discovery.

The key ideas underlying cold-atom spintronics—that studies particles with a synthetic spin degree of freedom coupled to their motion—grew out of the early theoretical work by Juzeliūnas *et al.* [6–12], which showed that single-particle physics of atom-laser dressed states, where internal atomic states are coupled by position-dependent laser fields, can be described in terms of a non-Abelian vector potential acting on the dressed excitations. Later, it was demonstrated theoretically [13] that specific realizations of such laser configurations, including the early-proposed tripod scheme, give rise to spin-orbit-coupled Hamiltonians of Rashba-Dresselhaus type, familiar from solid-state semiconductor spintronics, and that this "spintronics" description is a convenient alternative to the description in terms of the non-Abelian fields. Most importantly, it was quickly realized [14] that, contrary to solid-state spintronics, where the underlying particles are bound to be electronic excitations, the synthetic spin-1/2 degree of freedom in cold atoms can be carried by dressed spin-orbit-coupled bosons that were predicted to condense into a state, dubbed in Ref. [14] a "spin-orbit-coupled Bose-Einstein condensate (BEC)." It was also shown [14] that multiple peaks in the time-of-flight expansion would be a smoking-gun signature of such a new quantum state. Remarkably, this type of behavior was observed experimentally [2] by one of the authors shortly after. The specific laser setup used in Ref. [2]—that gives rise to a spin-orbit coupling of "persistent-spin-helix type" [15–21]—was later analyzed in detail by Ho and collaborators in Ref. [22]. These experimental and theoretical successes have motivated other interesting theoretical proposals for realistic experimental schemes that can be used to create spin-orbit-coupled systems [23,24]. Spin-orbit-coupled BECs have also been studied theoretically in Refs. [25–35] for different types of spin-orbit interactions and different internal structures of bosons (pseudospin-1/2, spin-1, and spin-2 bosons).

Among the obvious questions about the spin-orbit BECs is the physics of topological excitations (vortices) that play a central role in the physics of conventional BECs. This is subject of this paper, where we focus primarily on exploring experimentally relevant methods that can be used to nucleate static vortex structures in spin-orbit BECs. In contrast to the conventional condensates, the situation here is shown to be significantly more complicated as the vortex physics is obscured by the interplay of external perturbations intended to create them and the hyperfine structure underlying the synthetic spin-orbit-coupling setup.

It is widely known, and often taken for granted, that rotating a Bose-Einstein condensate gives rise to the formation of vortices that arrange themselves into static vortex lattice structures. However, this picture is not, in fact, an obvious outcome of rotation, which represents a *time-dependent perturbation* due to a rotating anisotropic trap potential. The many subtleties involved in understanding the fundamentals of the related phenomena are discussed in detail in the reviews by Leggett [36,37], but the main conclusion is indeed that the physics of a one-component BEC confined to a spinning anisotropic trap can be mapped onto a statistical-mechanical problem of the BEC with an effective *time-independent* Hamiltonian, $H_{\rm eff} = H - \boldsymbol{\omega}_r \cdot \mathbf{L}$, which describes the system in a rotating frame of reference (where $\mathbf{L}$ is the orbital angular momentum operator and $\boldsymbol{\omega}_r$ is the frequency of rotation).

A naïve expectation, therefore, is that to rotate an anisotropic trap would be a straightforward means to create vortex structures in spin-orbit-coupled BECs as well. However, this paper shows that this is *not so* and other, more sophisticated, methods have to be involved in order

 ©2011 American Physical Society

to create static vortex structures. We show that the problem with rotation arises here because atoms are not influenced by the trapping potential only but also by the lasers which create spin-orbit coupling in the first place. Therefore, if only the anisotropic potential rotates, it is, in general, impossible to choose a frame of reference where the Hamiltonian is time independent, because the "spin-orbit coupling" lasers, stationary in the laboratory frame, are rotating in the rotating frame, generally resulting in nontrivial dynamics in any rotating frame. While there do exist rare degenerate cases, where a unitary transformation can be found that eliminates time dependence from the noninteracting Hamiltonian, the interaction terms generally become time dependent under the unitary transformation, resulting, again, in a nonequilibrium problem. Hence, we argue that the residual time dependence appears to be an essential and unwelcome property of a spin-orbit-coupled BEC with rotating anisotropic potential (at least for the realistic laser schemes currently known to us). We believe that while the specifics of the time evolution of rotating spin-orbit BECs are sensitive to details of both the laser setup used and interactions, the typical scenario will involve nonuniversal dynamics that would inevitably lead to heating and destruction of the coherent state in contrast to the conventional BECs.

It is, therefore, desirable to develop other experimentally relevant methods to create vortices, like rotation or a magnetic field, for spin-orbit-coupled BECs. Two other ways suggested here and examined in detail are as follows: (i) to rotate both the lasers creating spin-orbit coupling and the trap, if the latter is anisotropic, or just the lasers for an isotropic trap (note that to rotate an isotropic trap has no meaning); and (ii) to combine synthetic spin-orbit couplings with a synthetic Abelian magnetic field. Theoretically, both methods are shown to give rise to interesting phenomena, including the appearance of sought-after static vortices and vortex lattices, parity effects in vortex nucleation, and real-space splitting of the spin-orbit BEC where the left- and right-moving parts are physically separated (an effect, which bears some similarity to the spin-Hall effect known in condensed matter spintronics).

Our paper is structured as follows: Section II derives effective Hamiltonians corresponding to a rotating trapping potential and/or rotating "spin-orbit lasers" for various spin-orbit-coupled laser schemes. In Sec. III, we solve the Gross-Pitaevskii equation to describe individual vortices and collective vortex structures for the laser scheme described in Ref. [4] with a rotating trap and Raman lasers. In Sec. IV, we investigate vortex nucleation and other effects associated with a synthetic magnetic field that can be imposed on top of the spin-orbit coupled system used in Ref. [4] by applying a spatially dependent Zeeman field.

II. ROTATION IN SYSTEMS WITH ENGINEERED SPIN-ORBIT COUPLING

In this section, we investigate the effect of rotation of an anisotropic trapping potential and/or spin-orbit lasers in three different laser schemes that have been proposed to create effective spin-orbit couplings. To distinguish between the different schemes, we will refer to the setup used in Ref. [4] as an "M scheme," the proposal described in Refs. [8,13] as "tripod scheme," and the recent proposal of Ref. [24] as a "four-level scheme."

A. M scheme

We, first, focus on the scheme used in recent experiment [4] and investigate the Hamiltonian for the case in which both trap and spin-orbit coupling lasers are rotating about the z axis. The atoms in Ref. [4] are under the influence of three external sources: the trapping potential, Raman lasers which create spin-orbit coupling, and the magnetic field which creates Zeeman splitting (aligned along $\hat{\mathbf{y}}$ direction). If we wanted to get a time-independent Hamiltonian in the rotating frame we would have to rotate trapping potential, Raman lasers, and the magnetic field. To make things easier it is possible to change direction of the magnetic field to be along the z axis, which makes rotation of magnetic field about the z axis unnecessary. If the change of the direction of magnetic field is accompanied by change in polarization of Raman lasers (the direction of lasers stays the same), the system is described by the same effective equations as in Ref. [4]. It is also important to note that, in the case of an isotropic trap, rotation of the trap has no effect and, in that case, rotating only the Raman lasers suffices. The stationary system is described by the following Hamiltonian (see methods in Ref. [4]):

$$\hat{H}_0 = \left[\frac{\hbar^2\hat{\mathbf{k}}^2}{2m} + V(\mathbf{r})\right]\check{1} + \begin{pmatrix} \hbar(-\omega_z+\omega_q) & 0 & 0 \\ 0 & 0 & 0 \\ 0 & 0 & \hbar\omega_z \end{pmatrix} + \sqrt{2}\Omega\check{\sigma}_{3,x}\cos(2k_L x + \Delta\omega_L t), \tag{1}$$

where $\hat{\mathbf{k}} = -i\nabla$, $V(\mathbf{r})$ is the trapping potential, $\check{1}$ is the 3×3 identity matrix, $\check{\sigma}_{3,x,y,z}$ are the 3×3 spin matrices, $k_L = \sqrt{2}\pi/\lambda$, Ω is the Raman coupling strength, ω_z and ω_q are the linear and quadratic Zeeman shifts, respectively. Here λ is the wavelength and $\Delta\omega_L$ is the frequency difference of the two Raman beams used in the M scheme. The Hamiltonian is written in the basis of hyperfine states $\{|m_F=+1\rangle, |m_F=0\rangle, |m_F=-1\rangle\}$ which are quantized in $\hat{z}$ direction (direction of the external magnetic field).

When the trap and Raman lasers rotate with a constant frequency ω_r about the z axis, the Hamiltonian $\hat{H}_{\rm rot}$ in the laboratory frame can be obtained from Eq. (1) using the following substitutions:

$$\begin{aligned} V(x,y,z) &\to V(x(t),y(t),z), \\ \check{\sigma}_{3,x}\cos(2k_L x + \Delta\omega_L t) &\to \check{\sigma}_{3,x}(t)\cos[2k_L x(t) + \Delta\omega_L t], \end{aligned} \tag{2}$$

where

$$\begin{aligned} x(t) &= x\cos(\omega_r t) + y\sin(\omega_r t), \\ y(t) &= y\cos(\omega_r t) - x\sin(\omega_r t), \\ \check{\sigma}_{3,x}(t) &= \check{\sigma}_{3,x}\cos(\omega_r t) + \check{\sigma}_{3,y}\sin(\omega_r t). \end{aligned} \tag{3}$$

The Hamiltonian $\hat{H}_{\rm rot}$ can be also written in a more compact form:

$$\hat{H}_{\rm rot} = e^{-i\omega_r t(\hat{L}_z+\hat{S}_z)/\hbar}\hat{H}_0 e^{i\omega_r t(\hat{L}_z+\hat{S}_z)/\hbar}, \tag{4}$$

where $\hat{\mathbf{L}}$ is the orbital angular momentum operator and $\hat{\mathbf{S}}$ is the spin operator and $\hat{L}_z$ and $\hat{S}_z$ are their z components: $\hat{L}_z = \hbar(x\hat{k}_y - y\hat{k}_x)\check{1}$, $\hat{S}_z = \hbar\check{\sigma}_{3,z}$.

The Hamiltonian (4) is time dependent in the laboratory frame, but we show below that this time dependence can be eliminated by a unitary transform. Recall that an arbitrary unitary transform, $\hat{U}(t)$, of the Hamiltonian $\hat{H}$ produces a new Hamiltonian, $\hat{H}'$, as follows:

$$\hat{H}' = \hat{U}\hat{H}\hat{U}^\dagger - i\hbar\hat{U}\frac{\partial\hat{U}^\dagger}{\partial t}. \tag{5}$$

We, first, go to the rotating frame of reference (rotating together with both the trap and the lasers) [38]: $|\psi_{\rm RF}\rangle = \hat{U}(t)|\psi\rangle$, where $\hat{U}(t) = \exp[i\omega_r t(\hat{L}_z + \hat{S}_z)/\hbar]$. Equation (5) yields

$$\hat{H}_{\rm RF} = \hat{H}_0 - \omega_r(\hat{L}_z + \hat{S}_z), \tag{6}$$

where $\hat{H}_{\rm RF}$ denotes the Hamiltonian in the rotating frame. The remaining time dependence, arising from the oscillating Raman laser fields in $\hat{H}_0$, can be removed in the framework of the rotating-wave approximation. To obtain an effective description of the system in terms of two internal pseudospin states, we follow Ref. [4] and choose the quadratic Zeeman shift $\hbar\omega_q$ to be large enough, so the state $|m_z = 1\rangle$ can be neglected. Using the pseudospin-1/2 labels for internal states, we get $|\uparrow\rangle \equiv |m_z = 0\rangle$ and $|\downarrow\rangle \equiv |m_z = -1\rangle$. The final Hamiltonian can be expressed in the form used in Ref. [4] (a detailed derivation is analogous to Ref. [4] and is presented in Appendix A) as follows:

$$\begin{aligned}\hat{H}_{\rm RF,2} = &\left[\frac{\hbar^2\hat{\mathbf{k}}^2}{2m} + V(\mathbf{r}) - \omega_r\hat{L}_z\right]\check{1} + \frac{\hbar^2 k_L}{m}\hat{k}_x\check{\sigma}_z \\ &+ \frac{\Omega}{2}\check{\sigma}_x + \hbar\omega_r k_L y\check{\sigma}_z + \begin{pmatrix} 0 & 0 \\ 0 & \hbar\omega_r - \delta \end{pmatrix},\end{aligned} \tag{7}$$

where $\check{1}$ is 2×2 unit matrix, $\check{\sigma}_{x,y,z}$ are 2×2 Pauli matrices, and $\delta = \hbar(\Delta\omega_L - \omega_z)$ is a detuning from the Raman resonance. Since the resulting Hamiltonian is time independent in the rotating frame, it leads to the appearance of stationary vortex structures studied below in Sec. III.

In the case where *only* the anisotropic trap is rotating, the Hamiltonian in the laboratory frame is given by Eq. (1), with $V(x,y,z) \to V(x(t),y(t),z)$. Importantly, if we go to the rotating frame and make the rotating-wave approximation (exactly as in the above), we are still left with a time dependence (for details see Appendix B):

$$\begin{aligned}\hat{H}'_{\rm RF,2} = &\left[\frac{\hbar^2\hat{\mathbf{k}}^2}{2m} + V(\mathbf{r}) - \omega_r\hat{L}_z\right]\check{1} \\ &+ \frac{\hbar^2 k_L}{m}\hat{k}_x(t)\check{\sigma}_z + \frac{\Omega}{2}\check{\sigma}_x + \frac{\delta}{2}\check{\sigma}_z,\end{aligned} \tag{8}$$

where $\hat{k}_x(t) = \hat{k}_x\cos(\omega_r t) - \hat{k}_y\sin(\omega_r t)$.

B. Tripod scheme

We now concentrate on the proposal described in Refs. [8, 13], which uses a so-called tripod scheme, which consists of three degenerate ground states of an atom coupled to an excited state. The resulting energy spectrum includes two degenerate "dark" states and two "bright" states (one of the bright states is higher and the other is lower in energy with respect to degenerate dark states). In the strong coupling regime and within the adiabatic approximation, the energy difference between the dark and bright states is very large compared to other characteristic energies of the system. In this case, a coupling between the dark and bright states is negligible, and, consequently, if the atoms initially exist within the dark states subspace, they are expected to stay there for a long time. From now on, we use pseudospin-1/2 notations for the two degenerate dark states.

The effective stationary Hamiltonian (projected onto the dark-state subspace) reads:

$$\hat{H} = \left[\frac{\hat{\mathbf{p}}^2}{2m} + w(\mathbf{r})\right]\check{1} - v_0\hat{p}_x\check{\sigma}_y - v_1\hat{p}_y\check{\sigma}_z + \delta_0\check{\sigma}_z, \tag{9}$$

where $\mathbf{p} = -i\hbar\nabla$, $w(\mathbf{r})$ is a spin-independent part of the trapping potential (see Appendix C for details), v_0 and v_1 characterize the strength and type of spin-orbit coupling, δ_0 is the effective Zeeman splitting, $\check{1}$ is a 2×2 unit matrix, and $\check{\sigma}_{x,y,z}$ are 2×2 Pauli matrices.

We, first, investigate the case with both the trap and the spin-orbit lasers rotating. The derivation, presented in Appendix C, leads to the following Hamiltonian in the rotating frame:

$$\begin{aligned}\hat{H}_{\rm RF,2} = &\left[\frac{\hat{\mathbf{p}}^2}{2m} + w(\mathbf{r}) - \omega_r\hat{L}_z\right]\check{1} - v_0\hat{p}_x\check{\sigma}_y - v_1\hat{p}_y\check{\sigma}_z \\ &+ \delta_0\check{\sigma}_z + m\hbar\omega_r(v_1 x\check{\sigma}_z - v_0 y\check{\sigma}_y) \\ &- \hbar\omega_r\begin{pmatrix} \sin^2\phi & \sin\phi\cos\phi\cos\theta \\ \sin\phi\cos\phi\cos\theta & \cos^2\theta\cos^2\phi - \sin^2\theta \end{pmatrix},\end{aligned} \tag{10}$$

where $\phi = mv_0 x/\cos\theta$, $\delta_0 = \sin^2\theta\{\delta - [(\frac{v_0}{\cos\theta})^2 + (\frac{v_1}{\sin^2(\theta/2)})^2]/2\}/2$, and θ is a constant. Let us note here that Ref. [39] previously considered the tripod scheme under rotation but obtained slightly different results (the spin angular momentum part $(-\omega_r\hat{S}_z)$ was ignored in Ref. [39]).

Our result [Eq. (10)], together with Eq. (7) for the M scheme, clearly shows that the effect of rotation in systems with synthetic spin-orbit interaction does not reduce to just adding the $-\omega_r L_z$ term for the Hamiltonian in the rotating frame but also produces other position-dependent terms, which depend on a particular scheme.

We now consider the tripod scheme with only the trap rotating. We, first, address the following question: If the trapping potential is time dependent, can we get the effective pseudospin Hamiltonian in the laboratory frame just by changing $V \to V(t)$ in Eq. (9); or, in other words, are we still allowed to restrict to the dark-state subspace if the external potential is time dependent? The answer is certainly yes, if the trapping potential is the same for all three degenerate ground states (which is most often the case for optical trapping), because this kind of time-dependent potential does not couple the dark and bright states.

In a general tripod scheme, however, the trapping potential is not spin independent [$\hat{V}(\mathbf{r}) = \sum_j V_j(\mathbf{r})|j\rangle\langle j|$, $V_1 = V_2 = w(\mathbf{r})$, and $V_3 = w(\mathbf{r}) + \delta$]. To better understand this case, let us choose states $\{|1\rangle,|2\rangle,|3\rangle\}$ to be eigenstates of $\hat{S}_z$ (z component of the total spin operator). The rotation of the trapping potential

about the z axis then is described by $V_1 = V_2 = w'(\mathbf{r},t)$ and $V_3 = w'(\mathbf{r},t) + \delta$, where $w'(\mathbf{r},t) = e^{-i\omega_r t \hat{L}_z/\hbar} w(\mathbf{r}) e^{i\omega_r t \hat{L}_z/\hbar}$. We can therefore separate $\hat{V}(\mathbf{r})$ into a stationary spin-dependent term and a time dependent but spin-independent term as follows: $\hat{V}(\mathbf{r},t) = \delta|3\rangle\langle 3| + w'(\mathbf{r},t)(|1\rangle\langle 1| + |2\rangle\langle 2| + |3\rangle\langle 3|)$. Therefore, the time-dependent part of the trapping potential is spin independent and it will not couple dark and bright states. With this, the tripod system with a trap rotating about the z axis is described by

$$\hat{H} = \left[\frac{\hat{\mathbf{p}}^2}{2m} + w'(\mathbf{r},t)\right]\check{1} - v_0\hat{p}_x\check{\sigma}_y - v_1\hat{p}_y\check{\sigma}_z + \delta_0\check{\sigma}_z. \quad (11)$$

We now make the transformation $\hat{U}(t) = \exp[i\omega_r t(\hat{L}_z/\hbar + \check{\sigma}_x/2)]$, which gives

$$\hat{H}' = \left[\frac{\hat{\mathbf{p}}^2}{2m} + w(\mathbf{r}) - \omega_r\hat{L}_z\right]\check{1} - v_0\hat{p}_x(t)\check{\sigma}_y(t) - v_1\hat{p}_y(t)\check{\sigma}_z(t) + \delta_0\check{\sigma}_z(t) - \frac{\hbar\omega_r}{2}\check{\sigma}_x, \quad (12)$$

where

$$\begin{aligned}\hat{p}_x(t) &= \hat{p}_x\cos(\omega_r t) - \hat{p}_y\sin(\omega_r t),\\ \hat{p}_y(t) &= \hat{p}_y\cos(\omega_r t) + \hat{p}_x\sin(\omega_r t),\\ \check{\sigma}_y(t) &= \check{\sigma}_y\cos(\omega_r t) - \check{\sigma}_z\sin(\omega_r t),\\ \check{\sigma}_z(t) &= \check{\sigma}_z\cos(\omega_r t) + \check{\sigma}_y\sin(\omega_r t).\end{aligned} \quad (13)$$

The Hamiltonian (12) is generally time dependent. However, in the case of Rashba coupling ($v_0 = v_1 = v$) and $\delta_0 = 0$, this *noninteracting part* of the Hamiltonian becomes static and reads

$$\hat{H}' = \left[\frac{\hat{\mathbf{p}}^2}{2m} + w(\mathbf{r}) - \omega_r\hat{L}_z\right]\check{1} - v(\hat{p}_x\check{\sigma}_y + \hat{p}_y\check{\sigma}_z) - \frac{\hbar\omega_r}{2}\check{\sigma}_x. \quad (14)$$

C. Four-level scheme

Here we study the four-level scheme [24] for the case where only the trap is rotating. The stationary effective Hamiltonian (projected to the lowest energy states) is given by Ref. [24]

$$\hat{H} = \left[\frac{\hbar^2\hat{\mathbf{k}}^2}{2m} + V(\mathbf{r})\right]\check{1} + \alpha(\check{\sigma}_x\hat{k}_y - \check{\sigma}_y\hat{k}_x) + \beta(\check{\sigma}_x\hat{k}_y + \check{\sigma}_y\hat{k}_x) + \frac{\Delta_z}{2}\check{\sigma}_z, \quad (15)$$

where α and β denote strengths of Rashba and Dresselhaus couplings, respectively (in this scheme, α is fixed and β can be tuned), and Δ_z is an effective Zeeman field. Per the same arguments as in the tripod scheme, we are allowed to simply replace $V \to V(t)$ in Eq. (15) (if an external potential is time dependent; note also that the trapping potential here is spin independent). The rotating trap potential reads $V(\mathbf{r},t) = e^{-i\omega_r t\hat{L}_z/\hbar}V(\mathbf{r})e^{i\omega_r t\hat{L}_z/\hbar}$. We now make the transformation $\hat{U}(t) = \exp[i\omega_r t(\hat{L}_z/\hbar + \check{\sigma}_z/2)]$, which gives

$$\hat{H}' = \left[\frac{\hbar^2\hat{\mathbf{k}}^2}{2m} + V(\mathbf{r}) - \omega_r\hat{L}_z\right]\check{1} + \alpha(\check{\sigma}_x\hat{k}_y - \check{\sigma}_y\hat{k}_x) + \beta\{[\check{\sigma}_y\cos(2\omega_r t) + \check{\sigma}_x\sin(2\omega_r t)]\hat{k}_x + [\check{\sigma}_x\cos(2\omega_r t) - \check{\sigma}_y\sin(2\omega_r t)]\hat{k}_y\} + \left(\frac{\Delta_z}{2} - \frac{\hbar\omega_r}{2}\right)\check{\sigma}_z. \quad (16)$$

Again, this *noninteracting part* of the Hamiltonian is, in general, time dependent; however, for pure Rashba coupling ($\beta = 0$), it becomes time independent.

Note that to get the full Hamiltonian in the rotating frame, we must also include interactions between the bosons and apply to them the same transformations as in the noninteracting part above. If both the trap and spin-orbit lasers rotate, the corresponding unitary operator, $\hat{U}(t) = \exp[i\omega_r t(\hat{L}_z + \hat{S}_z)/\hbar]$, describes a spatial rotation about the z axis. If the bare interactions are rotationally invariant, the interaction part of the Hamiltonian does not change in the rotating frame. In contrast to this result, however, if only the trap is rotating, the interactions will generally acquire time dependence as well (we have found a few very special cases—with serious constraints on the parameters of the system—where a unitary transform can be found that makes both the pure Rashba noninteracting part and interactions time independent, but whether these degenerate cases can be realized experimentally remains unclear at this stage).

III. CREATING VORTICES BY ROTATION

In the previous section, we have shown that the Hamiltonian for the M scheme in the presence of a rotating trap and Raman lasers becomes time independent in the rotating frame. Analogously with the physics of "ordinary" BEC under rotation, there will be thermal equilibration in the system and vortices will form in the condensate.

Let us assume that the trapping frequency in the $\hat{\mathbf{z}}$ direction ω_z is so large that the system is an effective 2D system, where the motion in the $\hat{\mathbf{z}}$ direction is effectively frozen (this can be achieved by applying a 1D optical lattice in the $\hat{\mathbf{z}}$ direction). We also assume the interaction part of the Hamiltonian to have the form:

$$\hat{H}_{\text{int}} = \int d^2r\left(\frac{1}{2}G_1\hat{\rho}_\uparrow^2 + \frac{1}{2}G_2\hat{\rho}_\downarrow^2 + G_{12}\hat{\rho}_\uparrow\hat{\rho}_\downarrow\right), \quad (17)$$

where G_1, G_2, and G_{12} are effective 2D interaction strengths and are related to the 3D interaction strengths $G_1 = G_1^{3D}/(\sqrt{2\pi}l_z)$, $G_2 = G_2^{3D}/(\sqrt{2\pi}l_z)$, and $G_{12} = G_{12}^{3D}/(\sqrt{2\pi}l_z)$, where $l_z = \sqrt{\hbar/(m\omega_z)}$. $\hat{\rho}_\uparrow$ and $\hat{\rho}_\downarrow$ are density operators for the $|\uparrow\rangle$ and $|\downarrow\rangle$ states (normal ordering of the corresponding creation/annihilation operators is implied).

We are interested in finding the ground-state configuration of bosons in a rotating system described by Eqs. (7) and (17). First, we have to make an assumption about the ground state and we assume below that (at the mean-field level) all atoms

occupy the same single-particle state described by the spinor wave function, $(\psi_\uparrow(\mathbf{r}),\psi_\downarrow(\mathbf{r}))$ (we also call it condensate wave function). The condensate wave function satisfies the Gross-Pitaevskii (GP) equations below:

$$\begin{aligned}\mu\psi_\uparrow &= \left[-\frac{\hbar^2}{2m}\nabla^2 - i\frac{\hbar^2 k_L}{m}\frac{\partial}{\partial x} + V(\mathbf{r}) - \omega_r(\hat{L}_z - \hbar k_L y) + NG_1|\psi_\uparrow|^2 + NG_{12}|\psi_\downarrow|^2\right]\psi_\uparrow + \frac{\Omega}{2}\psi_\downarrow \\ \mu\psi_\downarrow &= \left[-\frac{\hbar^2}{2m}\nabla^2 + i\frac{\hbar^2 k_L}{m}\frac{\partial}{\partial x} + V(\mathbf{r}) - \omega_r(\hat{L}_z + \hbar k_L y - \hbar) - \delta + NG_2|\psi_\downarrow|^2 + NG_{12}|\psi_\uparrow|^2\right]\psi_\downarrow + \frac{\Omega}{2}\psi_\uparrow,\end{aligned} \tag{18}$$

where N is the total number of particles and μ is the Lagrange multiplier associated with the constraint $\int d^2r(|\psi_\uparrow|^2 + |\psi_\downarrow|^2) = 1$ (it can be shown that μ has a physical meaning of chemical potential [36]). We solve the GP equations by using a norm-preserving imaginary time propagation method (see, for example, Refs. [38,40]).

We consider a trapping potential of the following form: $V = \frac{1}{2}m\omega^2(x^2 + \gamma^2 y^2)$, where ω and $\gamma\omega$ are trapping frequencies in the $\hat{\boldsymbol{x}}$ and $\hat{\boldsymbol{y}}$ direction. It is convenient to measure lengths in the units of the harmonic oscillator length, $a_0 = \sqrt{\hbar/(m\omega)}$, and energy in terms of $\hbar\omega$. We introduce the dimensionless position variable $\mathbf{r}' = \mathbf{r}/a_0$. The corresponding "dimensionless GP equations" read

$$\begin{aligned}\mu'\psi_\uparrow &= \left[-\frac{1}{2}\nabla'^2 - ik'_L\frac{\partial}{\partial x'} + \frac{1}{2}(x'^2 + \gamma^2 y'^2) - \omega'_r(\hat{L}'_z - k'_L y') + g_1|\psi_\uparrow|^2 + g_{12}|\psi_\downarrow|^2\right]\psi_\uparrow + \frac{\Omega'}{2}\psi_\downarrow \\ \mu'\psi_\downarrow &= \left[-\frac{1}{2}\nabla'^2 + ik'_L\frac{\partial}{\partial x'} + \frac{1}{2}(x'^2 + \gamma^2 y'^2) - \delta' - \omega'_r(\hat{L}'_z + k'_L y' - 1) + g_2|\psi_\downarrow|^2 + g_{12}|\psi_\uparrow|^2\right]\psi_\downarrow + \frac{\Omega'}{2}\psi_\uparrow,\end{aligned} \tag{19}$$

where $k'_L = k_L a_0$, $\Omega' = \Omega/(\hbar\omega)$, $\delta' = \delta/(\hbar\omega)$, $\mu' = \mu/(\hbar\omega)$, $\omega'_r = \omega_r/\omega$, $\hat{L}_z = -i(x'\partial_{y'} - y'\partial_{x'})$, $g_1 = NG_1/(\hbar\omega a_0^2)$, $g_2 = NG_2/(\hbar\omega a_0^2)$, and $g_{12} = NG_{12}/(\hbar\omega a_0^2)$.

In simulations for the rotating system we consider ^{87}Rb atoms and we use the following experimentally relevant parameters: $\lambda = 804.1$ nm, $\omega = 2\pi \times 50$ Hz, and $\gamma = 1$. These parameters give $a_0 = \sqrt{\hbar/m\omega} = 1.52$ μm, $k'_L = 8.42$. From now on we express position and momentum in terms of dimensionless variables $\mathbf{r}' = \mathbf{r}/a_0$ and $\mathbf{k}' = \mathbf{k}a_0$ [coordinates (x,y) and (k_x,k_y) in figures are also dimensionless].

We performed simulations specifically for the rotation frequency $\omega_r = 0.7\,\omega$ and for three different coupling strengths: no coupling ($\Omega = 0$), weak coupling ($\Omega = 2E_L$), and strong coupling ($\Omega = 10E_L$), where $E_L = \hbar^2 k_L^2/2m$ is the recoil energy ($E_L = 35.4\hbar\omega$). In simulations we choose $g_1 = 1000$, $g_2 = 995$, and $g_{12} = 995$. The ratio among g_1, g_2, and g_{12} corresponds to interaction coefficients in ^{87}Rb (the interaction coefficients for ^{87}Rb in states $\{|F = 1,m = 0\rangle, |F = 1,m = -1\rangle\}$ are given in Ref. [4]). If we assume $\omega_z = 2\pi \times 2$ kHz, the number of particles corresponding to chosen interaction coefficients is $N \approx 10^4$. In the case without Raman coupling, rotation and with zero detuning ($\delta = 0$) the chemical potential is $\mu/h = 900$ Hz. In our simulations we set $\delta - \hbar\omega_r = 0$.

Without rotation and spin-orbit coupling, $|\uparrow\rangle$ and $|\downarrow\rangle$ components are miscible for our choice of interaction parameters. In the case of rotation and no spin-orbit coupling there are several different phases depending on ω_r and ratio of interaction coefficients [41]: triangular lattice, square lattice, stripe or double-core vortex lattice, and vortex sheet. Since our Hamiltonian is almost equivalent to the Hamiltonian in Ref. [41] for $\Omega = 0$ and $\delta - \hbar\omega_r = 0$ [there is a very small difference in the interaction coefficients; the equivalence of the noninteraction part of the two systems is clear from Eq. (A3)], we reproduced the results of Ref. [41].

The results for $\Omega = 0$ are shown in Fig. 1(a), which displays the densities of the $|\uparrow\rangle$ and $|\downarrow\rangle$ components forming spatially separated density stripes with lines of vortices along the minima of the density. As expected, our results reproduce the stripe vortex lattice phase described in Ref. [41]. Note that for $\Omega = 0$, the Hamiltonian (7) conserves number of the $|\uparrow\rangle$ and $|\downarrow\rangle$ particles separately. We have chosen $N_\uparrow = N_\downarrow$ ($N_i = \int d^2r|\psi_i|^2$). A weak spin-orbit coupling ($\Omega = 2E_L$) [Fig. 1(b)] does not appear to lead to significant qualitative changes in the observed behavior: The densities of the $|\uparrow\rangle$ and $|\downarrow\rangle$ components are still spatially separated and there are lines of vortices along the density minima of each component.

A significant change comes in the strong-coupling regime: see the $\Omega = 10E_L$ data shown in Fig. 1(c). The vortices arrange themselves in a lattice in the $|\uparrow\rangle$ and $|\downarrow\rangle$ components and densities of both components are almost identical. This behavior can be understood from the following part of the Hamiltonian (7):

$$\hat{H}' = \frac{\hbar^2\hat{k}_x^2}{2m}\check{1} + \frac{\hbar^2 k_L\hat{k}_x}{m}\check{\sigma}_z + \frac{\Omega}{2}\check{\sigma}_x. \tag{20}$$

The spectrum of Eq. (20) for different Ωs is shown in Fig. 2(a). For large Ω, it consists of two bands with an energy separation much larger than all other characteristic energies of the system. Therefore, our system is "confined" to the lower band with a single minimum, which effectively makes it a single-component system. This explains almost identical densities of the two components in Fig. 1(c).

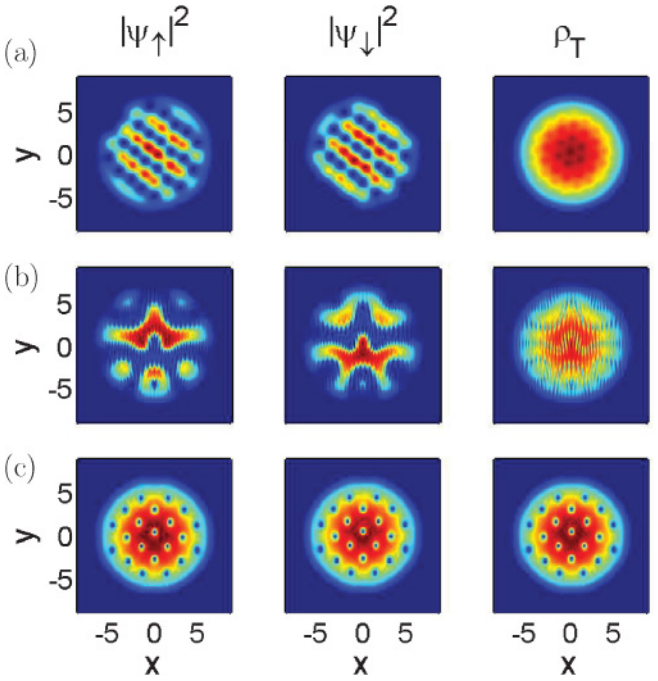

FIG. 1. (Color online) The density profiles for the rotating spin-orbit-coupled BEC are shown. The first, second, and third columns show density of the $|\uparrow\rangle$ component ($|\psi_\uparrow|^2$), density of the $|\downarrow\rangle$ component ($|\psi_\downarrow|^2$), and the total density ($\rho_T = |\psi_\uparrow|^2 + |\psi_\downarrow|^2$), respectively. (a) Results for $\Omega = 0$ which are characterized by density stripes and lines of vortices in both components. The results for $\Omega = 2E_L$ (b) are qualitatively similar to the $\Omega = 0$ case. (c) Results for $\Omega = 10E_L$; a vortex lattice is formed in both components and densities of the two components are almost identical.

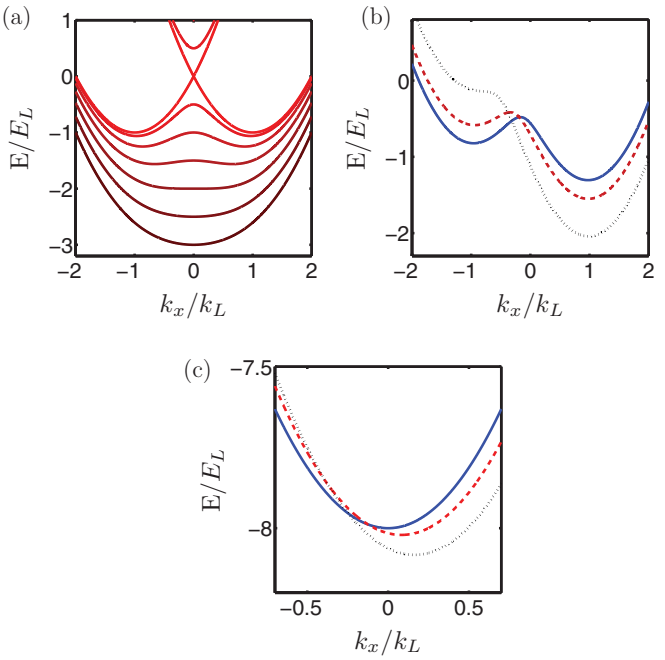

FIG. 2. (Color online) The energy spectrum of $\hat{H}'$ [Eq. (23)]. (a) Spectra for different Ω (from $\Omega = 0$ to $\Omega = 6E_L$) and $\delta = 0$ (spectrum for $\Omega = 0$ is at the top while spectrum for $\Omega = 6E_L$ is at the bottom). (b) The effect of δ in small Ω regime is shown [$\Omega = 1E_L$, $\delta = 0.5E_L$ (solid blue line), $\delta = 1E_L$ (dashed red line), and $\delta = 2E_L$ (dotted black line)]. (c) The effect of δ in the large Ω regime is shown [$\Omega = 16E_L$, $\delta = 0E_L$ (solid blue line), $\delta = 1E_L$ (dashed red line), and $\delta = 2E_L$ (dotted black line)]. δ changes position and energy of the minimum.

IV. CREATING VORTICES BY SPATIALLY DEPENDENT DETUNING

A. The model

Vortices in spin-orbit systems like Ref. [4] can be created without any rotation but by imposing an additional synthetic magnetic field. In Ref. [42], it has been shown that a spatially dependent detuning, δ, in the M scheme results in a synthetic magnetic field, which creates vortices in the strong Raman coupling (Ω) regime. Our goal is to investigate the same system for a wide range of Ω (from weak to strong Raman coupling) and to see what kind of vortex structures it yields.

The setup is described by the effective Hamiltonian (see Refs. [4,42])

$$\hat{H} = \left[\frac{\hbar^2\hat{\mathbf{k}}^2}{2m} + V(\mathbf{r})\right]\check{1} + \frac{\hbar^2 k_L \hat{k}_x}{m}\check{\sigma}_z + \frac{\Omega}{2}\check{\sigma}_x + \frac{\delta(y)}{2}\check{\sigma}_z, \quad (21)$$

where a spatially dependent $\delta(y)$ can be created in a laboratory by applying a spatially dependent magnetic field (see Ref. [3]) or by using the vector light shift.

We, again, assume strong confinement in the $\hat{z}$ direction and describe interactions by Eq. (17). We are looking for the ground state in the same way as in the rotating case and, following the same steps, we get the "dimensionless GP equations" as follows:

$$\begin{aligned}\mu'\psi_\uparrow &= \left[-\frac{1}{2}\nabla'^2 - ik'_L\frac{\partial}{\partial x'} + \frac{1}{2}(x'^2 + \gamma^2 y'^2)\right.\\ &\quad \left. + \frac{\delta'(y')}{2} + g_1|\psi_\uparrow|^2 + g_{12}|\psi_\downarrow|^2\right]\psi_\uparrow + \frac{\Omega'}{2}\psi_\downarrow\\ \mu'\psi_\downarrow &= \left[-\frac{\hbar^2}{2m}\nabla'^2 + ik'_L\frac{\partial}{\partial x'} + \frac{1}{2}(x'^2 + \gamma^2 y'^2)\right.\\ &\quad \left. - \frac{\delta'(y')}{2} + g_2|\psi_\downarrow|^2 + g_{12}|\psi_\uparrow|^2\right]\psi_\downarrow + \frac{\Omega'}{2}\psi_\uparrow.\end{aligned} \quad (22)$$

Parameters $\Omega', \delta', k'_L, g_1, g_2, g_{12}$ are defined in the same way as in Eq. (19). Equations (22) are solved using the same method as in Sec. III.

B. Qualitative discussion

To get a better understanding of the model, we investigate Hamiltonian (21) in more detail. It is instructive to first focus on the following part of Eq. (21):

$$\hat{H}' = \frac{\hbar^2\hat{k}_x^2}{2m}\check{1} + \frac{\hbar^2 k_L \hat{k}_x}{m}\check{\sigma}_z + \frac{\Omega}{2}\check{\sigma}_x + \frac{\delta}{2}\check{\sigma}_z. \quad (23)$$

We first assume that δ is constant in space. In that case, Hamiltonian (23) can be easily diagonalized in the momentum basis, $U^\dagger(k_x)H'(k_x)U(k_x) = \left(\begin{smallmatrix} E_+(k_x) & 0 \\ 0 & E_-(k_x)\end{smallmatrix}\right)$. The resulting spectrum consists of an upper(+) and lower(−) band, as shown in

Fig. 2. The gap separating the bands is large compared to other characteristic energies of the system and it is safe to assume that the condensate occupies only the states in the lower band. In Fig. 2(a), spectra for different coupling strengths Ω and $\delta = 0$ are shown. For $\Omega < 4E_L$, the spectrum has two minima and BEC will involve states near both left and right minima. At $\Omega = 4E_L$, there is a transition from a spectrum with two minima to a spectrum with one minimum, which changes the structure of the condensate wave function, i.e., for $\Omega > 4E_L$, the BEC is expected to occupy only states with momentum around $k_x = 0$.

The effect of detuning δ in the low-Ω regime is shown in Fig. 2(b). We see that δ shifts the energies and positions of the left and right minima. In the case of constant δ, the BEC would occupy only the states around the global minimum [for example, the right minimum in Fig. 2(b)]. Those cases have been tested experimentally in Ref. [4].

We now consider a spatially dependent $\delta(y)$. We consider it to be a linear function of y: $\delta(y) = \delta_0 + \beta y$, which is the simplest and the most experimentally relevant regime. The interesting physics is evident from the following arguments: For constant detuning, the spectrum around a minimum can be simply described by [we use dimensionless variables, see Eq. (19)] $(k_x - k_{\min})^2/(2m_{\text{eff}}) + E_{\min}$, where m_{eff}, $k_{\min}$, and $E_{\min}$ are the effective mass, position of the minimum, and the energy at the minimum, respectively. Note that all these quantities depend on δ. If δ is y dependent, the values of m_{eff}, $k_{\min}$, and $E_{\min}$ will also become spatially dependent. Hence, the spectrum around the minimum can now be written as $[k_x - k_{\min}(y)]^2/(2m_{\text{eff}}(y)) + E_{\min}(y)$, which describes particles moving in an effective gauge field $(\mathbf{A}, \Phi) = (k_{\min}(y), 0, 0, E_{\min}(y))$ with a spatially varying effective mass $m_{\text{eff}}(y)$ [42]. The spatially dependent vector potential $\mathbf{A}$ induces an effective magnetic field ($\mathbf{B}_{\text{eff}} = \nabla \times \mathbf{A}$), which may lead to creation of vortices if strong enough. This approximation provides a good description of the system only if the particles at some point y have the momentum k_x near the minimum. Our numerical simulations presented below indicate that this approximation in fact gives a very good qualitative description in a wide parameter range.

We calculate parameters $m_{\text{eff}}(y)$, $k_{\min}(y)$, and $E_{\min}(y)$ by diagonalizing (23) for different y's since $\delta = \delta(y)$. The procedure of deriving effective equations for the lower band for Hamiltonian (21) in the high Ω (single minimum) regime is described in Ref. [42]. Let us note, however, that the method we use to find the ground state, i.e., numerically solving Eqs. (22), is exact (in particular, we do not limit our system to the lower band and we do not simplify interaction terms).

C. Results

In simulations for a system with a spatially dependent detuning δ we use the same experimental parameters as in the simulations of a rotating system, which gives $a_0 = \sqrt{\hbar/(m\omega)} = 1.52\ \mu$m and $k'_L = 8.42$. We choose the interaction parameters to be $g_1 = 1600$, $g_2 = 1593$, and $g_{12} = 1593$ and the constant part of detuning $\delta_0 = 0$.

The results for $\Omega = 0$, $\beta = 4\hbar\omega/a_0$, and $\gamma = 1$ are shown in Fig. 3. Here we have chosen $N_\uparrow = N_\downarrow$ since for $\Omega = 0$ the Hamiltonian conserves the number of $|\uparrow\rangle$ and $|\downarrow\rangle$ particles

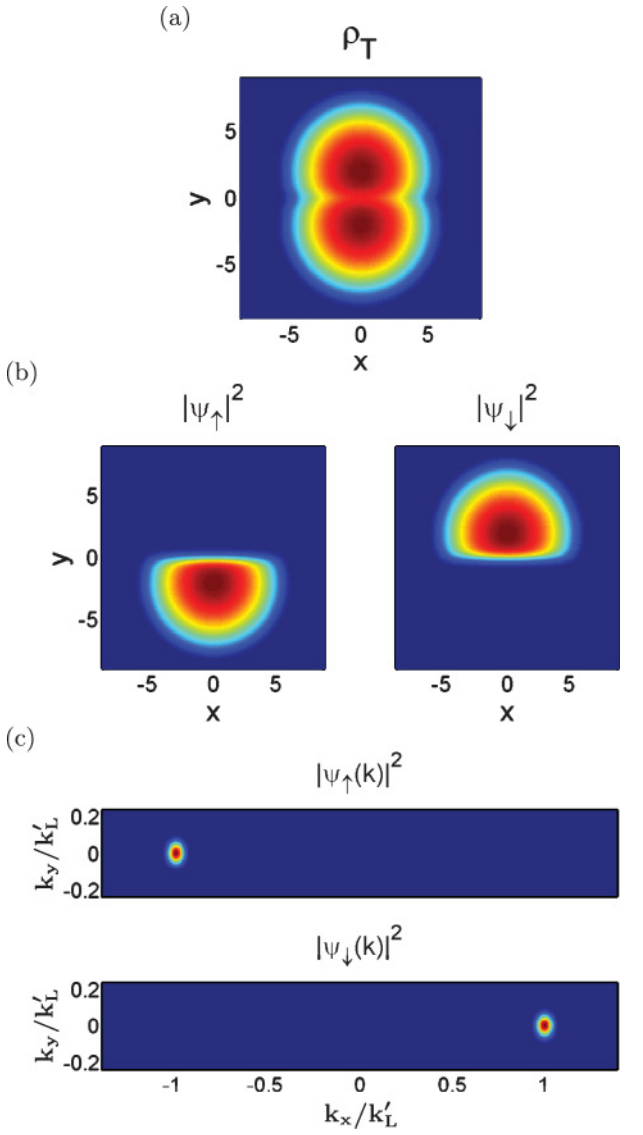

FIG. 3. (Color online) The figure shows results for $\Omega = 0$, $\beta = 4\hbar\omega/a_0$, and $\gamma = 1$. (a) The total density is shown. The shape of the density is determined by spatially dependent detuning, which shifts the densities of $|\uparrow\rangle$ and $|\downarrow\rangle$ particles (b). Momentum distribution of the $|\uparrow\rangle$ and $|\downarrow\rangle$ components is shown in (c).

separately. The results are straightforward, i.e., in this case, we may write the Hamiltonian (21) as

$$\hat{H} = \begin{pmatrix} H_\uparrow & 0 \\ 0 & H_\downarrow \end{pmatrix},$$

where $H_\uparrow = \frac{\hbar^2}{2m}(\hat{\mathbf{k}}^2 + 2k_L\hat{k}_x) + V_\uparrow(\mathbf{r})$, $H_\downarrow = \frac{\hbar^2}{2m}(\hat{\mathbf{k}}^2 - 2k_L\hat{k}_x) + V_\downarrow(\mathbf{r})$, and $V_\uparrow(\mathbf{r}) = V(\mathbf{r}) + \delta(y)/2$, $V_\downarrow(\mathbf{r}) = V(\mathbf{r}) - \delta(y)/2$. We see that the motion of the $|\uparrow\rangle$ and $|\downarrow\rangle$ particles is decoupled in $\hat{H}$ and that they experience different potentials $V_\uparrow(\mathbf{r})$, $V_\downarrow(\mathbf{r})$. Detuning gradient β shifts the minima of $V_\uparrow(\mathbf{r})$ [$V_\downarrow(\mathbf{r})$] for $y_0 = \beta/(2m\omega^2\gamma^2)$ in the positive [negative] $\hat{\mathbf{y}}$ direction and, therefore, the centers of the $|\uparrow\rangle$ and $|\downarrow\rangle$ densities are shifted from the origin by $\pm y_0$ [the origin is located in the minimum of $V(\mathbf{r})$]; see Fig. 3(b). Also, it is clear from $\hat{H}$ and Fig. 2(a) that the momentum distribution of

the $|\uparrow\rangle$ [$|\downarrow\rangle$] particles will be centered around $\mathbf{k} = (-k_L,0)$ [$\mathbf{k} = (k_L,0)$]; see Fig. 3(c) (in dimensionless units k_L is simply replaced by k'_L). The effect of repulsive interactions between the particles with different spins is clearly seen (the overlap between $|\uparrow\rangle$ and $|\downarrow\rangle$ densities is quite small).

If we introduce a finite Ω, the Hamiltonian becomes $\hat{H} = \left(\begin{smallmatrix} H_\uparrow & \Omega/2 \\ \Omega/2 & H_\downarrow \end{smallmatrix}\right)$, and the corresponding Ω term creates coupling between the $|\uparrow\rangle$ and $|\downarrow\rangle$ particles. If $\delta = \text{const} = 0$ and Ω is small, the states around the left [right] minimum in the spectrum in Fig. 2(a) still consist mainly of the $|\uparrow\rangle$ [$|\downarrow\rangle$] particles, but there is also some admixture of the component with the opposite spin, which grows with Ω. It means that $\psi_\uparrow(\mathbf{r})$ [$\psi_\downarrow(\mathbf{r})$] will mainly consist of states with momentum around the left [right] minimum but also of states around the right [left] minimum. We can therefore write:

$$\begin{pmatrix} \psi_\uparrow(\mathbf{r}) \\ \psi_\downarrow(\mathbf{r}) \end{pmatrix} = \begin{pmatrix} \psi_{\uparrow L}(\mathbf{r}) \\ \psi_{\downarrow L}(\mathbf{r}) \end{pmatrix} + \begin{pmatrix} \psi_{\uparrow R}(\mathbf{r}) \\ \psi_{\downarrow R}(\mathbf{r}) \end{pmatrix}, \tag{24}$$

where $\psi_{\uparrow L}(\mathbf{r})$ and $\psi_{\downarrow L}(\mathbf{r})$ consist only of states with momenta around left peak, while $\psi_{\uparrow R}(\mathbf{r})$ and $\psi_{\downarrow R}(\mathbf{r})$ consist only of the states with momenta around right peak of momentum distribution. We therefore call $(\psi_{\uparrow L}(\mathbf{r}),\psi_{\downarrow L}(\mathbf{r}))$ and $(\psi_{\uparrow R}(\mathbf{r}),\psi_{\downarrow R}(\mathbf{r}))$ the left and right wave functions. In the spatially dependent detuning case it may happen that the momentum distribution is separated into two peaks (i.e., there exist "left movers" and "right movers") even for $\Omega > 4E_L$. In that case also the notion of the left and right wave functions applies.

To investigate the effect of Ω, which couples the $|\uparrow\rangle$ and $|\downarrow\rangle$ states, we consider the regime with $\Omega = 3\,E_L$ and $\beta = 8\hbar\omega/a_0$ (Fig. 4). The total density $\rho_T(\mathbf{r})$ is shown in Fig. 4(a) and there is a characteristic series of minima along the $\hat{x}$ direction at $y = 0$, which come from vortices in the $\psi_\uparrow$ and $\psi_\downarrow$ wave functions, see Fig. 4(b), which are positioned along x and near $y = 0$. We have checked that the phase winding around the zero density points of $\psi_\uparrow$ and $\psi_\downarrow$ is -2π. Since the vortices in the $|\downarrow\rangle$ and $|\uparrow\rangle$ components are slightly displaced from $y = 0$, the density at minima in ρ_T is close to, but not exactly equal to zero.

To explain the existence of the line of vortices in the $|\uparrow\rangle$ and $|\downarrow\rangle$ components, we examine the left and right wave functions. Figure 5(a) displays $|\psi_{\uparrow L}|^2$ and $|\psi_{\uparrow R}|^2$ (note that the amplitude of $\psi_{\uparrow R}$ is considerably smaller than the amplitude of $\psi_{\uparrow L}$: $\int d^2r|\psi_{\uparrow R}|^2 = 0.05$ and $\int d^2r|\psi_{\uparrow L}|^2 = 0.45$). The momentum distribution in Fig. 4(c) shows that the wave packet, $\psi_{\uparrow L}$, has an average momentum of $k_{\text{left}} = -0.8k'_L$ and $\psi_{\uparrow R}$ has an average momentum of $k_{\text{right}} = 0.8k'_L$. Since $\psi_\uparrow$ is a superposition of the left and right movers, $\psi_\uparrow = \psi_{\uparrow L} + \psi_{\uparrow R}$, the appearance of the line of vortices at overlapping region is expected. The separation of vortices d is then simply given by $(k_{\text{right}} - k_{\text{left}})d = 2\pi$ or $d = 2\pi/(k_{\text{right}} - k_{\text{left}})$. The analytical expression for d fits our numerical data perfectly well.

To explain the density profile and momentum distribution, it is useful to consider an effective gauge-field picture. The effective gauge field, $(\mathbf{A},\Phi) = (k_{\min}(y),0,0,E_{\min}(y))$, can be calculated by diagonalizing H', and we adopt the following corresponding notation: $A(y) = k_{\min}(y)$ and $\Phi(y) = E_{\min}(y)$. As discussed earlier, we may approximate the low-energy band physics by the following Hamiltonian (we use again

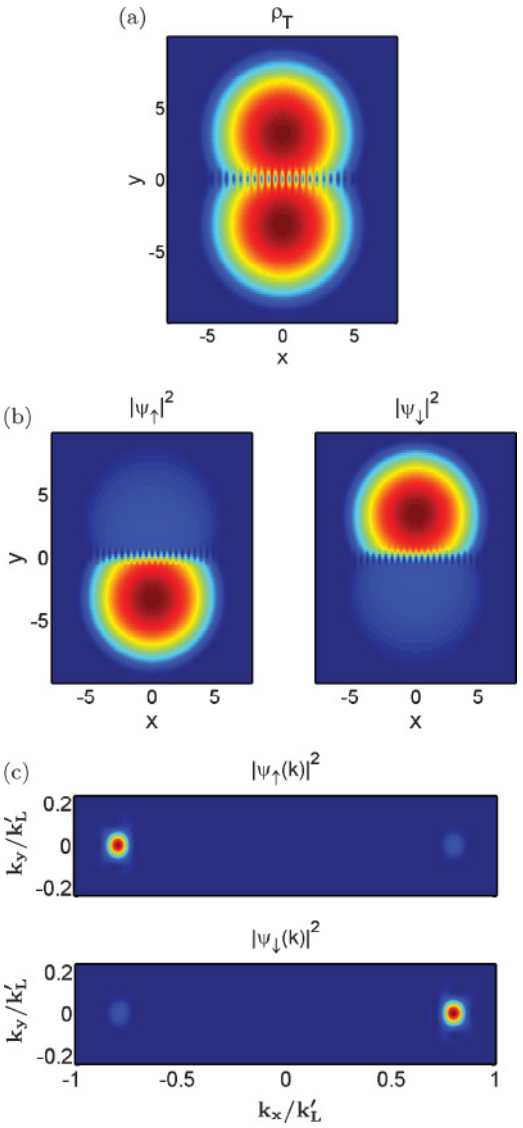

FIG. 4. (Color online) The figure shows results for $\Omega = 3E_L$, $\beta = 8\hbar\omega/a_0$, and $\gamma = 1$. (a) The total density is shown. The series of minima at $y = 0$ comes from vortices in the $|\uparrow\rangle$ and $|\downarrow\rangle$ wave functions (b). Momentum distribution of $|\uparrow\rangle$ and $|\downarrow\rangle$ components is shown in (c).

the dimensionless variables, where the lengths are measured in terms of a_0 and the wave vectors, k, in terms of $1/a_0$):

$$\hat{H}_{\text{EGF}} = \frac{1}{2m_{\text{eff}}(y)}[k_x - A(y)]^2 + \frac{1}{2}k_y^2 + \Phi(y) + V(\mathbf{r}), \tag{25}$$

where $V(\mathbf{r}) = \frac{1}{2}(x^2 + \gamma^2 y^2)$. For $\Omega \geqslant 4E_L$ there is a single local minimum in lower band of the Hamiltonian (23) spectrum for any δ. For $\Omega < 4E_L$ the spectrum has two minima for $\delta = 0$; however, when δ becomes large enough the spectrum has a single local minimum [Fig. 2(b)]. The spectrum around each local minimum can be approximated by the form given in Eq. (25), and, therefore, there will be $A_L(y)$, $\Phi_L(y)$, $m_{\text{eff,L}}(y)$ corresponding to the left minimum and $A_R(y)$, $\Phi_R(y)$, $m_{\text{eff,R}}(y)$ corresponding to the right minimum of the spectrum. Left-movers feel the "left gauge field"

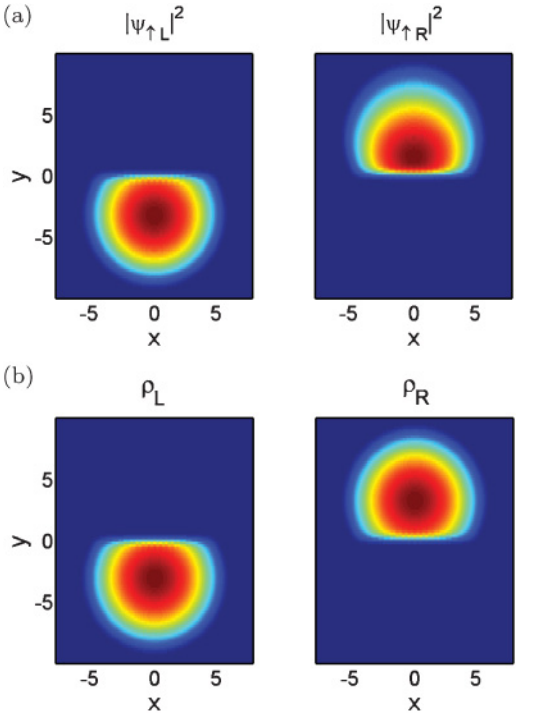

FIG. 5. (Color online) (a) Diagrams of $|\psi_{\uparrow L}|^2$ and $|\psi_{\uparrow R}|^2$, the relative amplitude of which is given by $\int d^2r|\psi_{\uparrow L}|^2 = 0.45$ and $\int d^2r|\psi_{\uparrow R}|^2 = 0.05$ for the parameters $\Omega = 3E_L$, $\beta = 8\hbar\omega/a_0$, and $\gamma = 1$. The superposition of $\psi_{\uparrow L}$ and $\psi_{\uparrow R}$, $\psi_{\uparrow} = \psi_{\uparrow L} + \psi_{\uparrow R}$, produces vortices in $\psi_{\uparrow}$. (b) The density of left- and right-moving particles ($\rho_L = |\psi_{\uparrow L}|^2 + |\psi_{\downarrow L}|^2$, $\rho_R = |\psi_{\uparrow R}|^2 + |\psi_{\downarrow R}|^2$) particles.

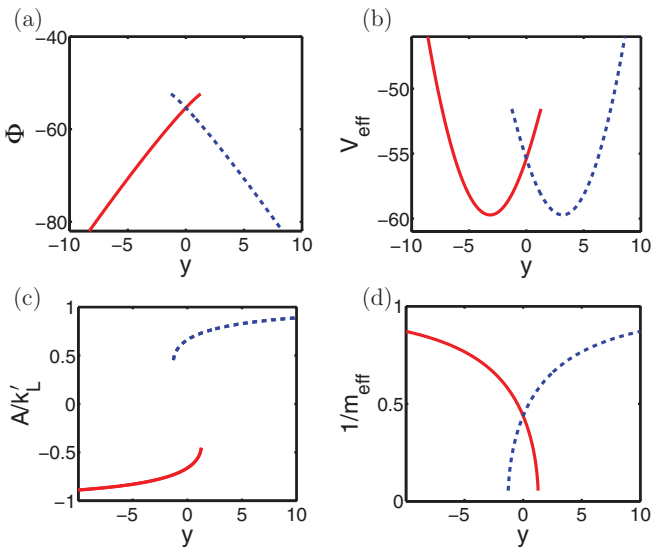

FIG. 6. (Color online) The scalar potential $\Phi(y)$ (a), the effective trapping potential in the $\hat{y}$ direction $V_{\rm eff}(y)$ (b), the vector potential $A(y)$ (c), and the inverse of the effective mass (d) for $\Omega = 3E_L$, $\beta = 8\hbar\omega/a_0$, and $\gamma = 1$. Values corresponding to the left minimum of the spectrum are represented by a solid red line while the values corresponding to the right minimum of the spectrum are represented by a dashed blue line (see the text for details).

$(A_L(y),0,0,\Phi_L(y))$ while right-movers feel the "right gauge field" $(A_R(y),0,0,\Phi_R(y))$.

To get the effective potential in the $\hat{y}$ direction acting on left and right movers we define $V_{\rm eff,L}(y) = \Phi_L(y) + \frac{1}{2}\gamma^2y^2$ and $V_{\rm eff,R}(y) = \Phi_R(y) + \frac{1}{2}\gamma^2y^2$. In Fig. 6 we show $\Phi_{L|R}(y)$, $V_{\rm eff,L|R}(y)$, $A_{\rm L|R}(y)$, and $1/m_{\rm eff,L|R}(y)$ for $\Omega = 3E_L$ and $\beta = 8\hbar\omega/a_0$. $V_{\rm eff,L|R}$ have minima at $y_{0,R|L} = \pm 3.2$ which explains the total density profile [Fig. 4(a)] which has maxima at $y = \pm 3.2$. The position of two peaks in momentum distribution in Fig. 4(c) can be understood as follows: for particles positioned near the minimum of $V_{\rm eff,L}$ in Fig. 6(b), it is energetically favorable to have the $\hat{x}$ component of momentum approximately equal to $A_L(y_{0,L})$ and the $\hat{y}$ component near zero [see Eq. (25)]. Figure 6(c) shows that $A_L(y_{0,L}) \approx -0.79k'_L$, while from Fig. 4(c), we see that the momentum distribution is centered around $k_x = -0.80k'_L$. The same explanation applies for the momentum distribution of right movers.

To investigate the regime with a single minimum in the spectrum ($\Omega \geqslant 4E_L$) we did calculations for the following parameters: $\Omega = 5E_L$, $\beta = 12\hbar\omega/a_0$, and $\gamma = 1$ (Fig. 7). In this "single-minimum" case one might expect the momentum distribution to be concentrated around a single point as was observed in Ref. [4]. However, in the spatially dependent detuning case, this is not necessarily true: The momentum distribution [Fig. 7(c)] shows two peaks around $k_x = \pm 0.55k'_L$. Also, the total density [Fig. 7(a)] has a characteristic series of minima along the $y = 0$ line which come from vortices in the $\psi_{\uparrow}$ and $\psi_{\downarrow}$ wave functions [Fig. 7(b)] created in the overlapping region of the left and right movers. The results can, again, be explained by the effective gauge field. The effective potential in the $\hat{y}$ direction $V_{\rm eff}(y) = \Phi(y) + \frac{1}{2}\gamma^2y^2$ [Fig. 8(a)] has two minima at $y_{0,R|L} = \pm 3.4$ which explains the density distribution which has maxima at $y = \pm 3.3$. Moreover, Eq. (25) tells us it is energetically favorable for particles near the left (right) minimum of $V_{\rm eff}(y)$ to have momentum around $A(y_{0,L}) = -0.56k'_L$ [$A(y_{0,R}) = 0.56k'_L$] [Fig. 8(c)] which explains momentum distribution. We also note that in Fig. 8(c) $A(y)$ has a large gradient and, therefore, the magnetic field ($B_{\rm eff} \sim \partial A/\partial y$) is strong around $y = 0$ which may serve as an alternative explanation of line of vortices appearing in Fig. 7(a).

We now study the system with strong Raman coupling Ω and weak detuning gradient β (i.e., β is not large enough to produce spatial separation of a cloud along $\hat{y}$ as in previous cases). Results for $\Omega = 10E_L$ and $\beta = 12\hbar\omega/a_0$ are shown in Fig. 9 and can be explained by the associated effective gauge field shown in Fig. 10. The total density [Fig. 9(a)] and $|\psi_{\uparrow}|^2$, $|\psi_{\downarrow}|^2$ [Fig. 9(b)] show the existence of a vortex in the center of the cloud. The vortex appears only for strong-enough effective magnetic field which is tuned by changing β. We define the effective magnetic field $\mathbf{B}_{\rm eff} = \nabla \times \mathbf{A}(y)$ and in our case, $\mathbf{A} = (A(y),0,0)$, $\mathbf{B}_{\rm eff} = -\frac{\partial A(y)}{\partial y}\hat{z}$. The magnetic field points in the $\hat{z}$ direction, depends on y, and is constant along x. We also note that since $m_{\rm eff}(y) \neq 1$ [Fig. 10(d)], the effective equations will differ from those for an ordinary charged particle in a magnetic field $B_{\rm eff}(y)\hat{z}$. The vector potential $A(y)$ and the effective magnetic field $\mathbf{B}_{\rm eff}(y)$ are shown in Figs. 10(b) and 10(c).

It is useful to know the critical field needed for vortex creation and we may get a crude estimate by using the equation

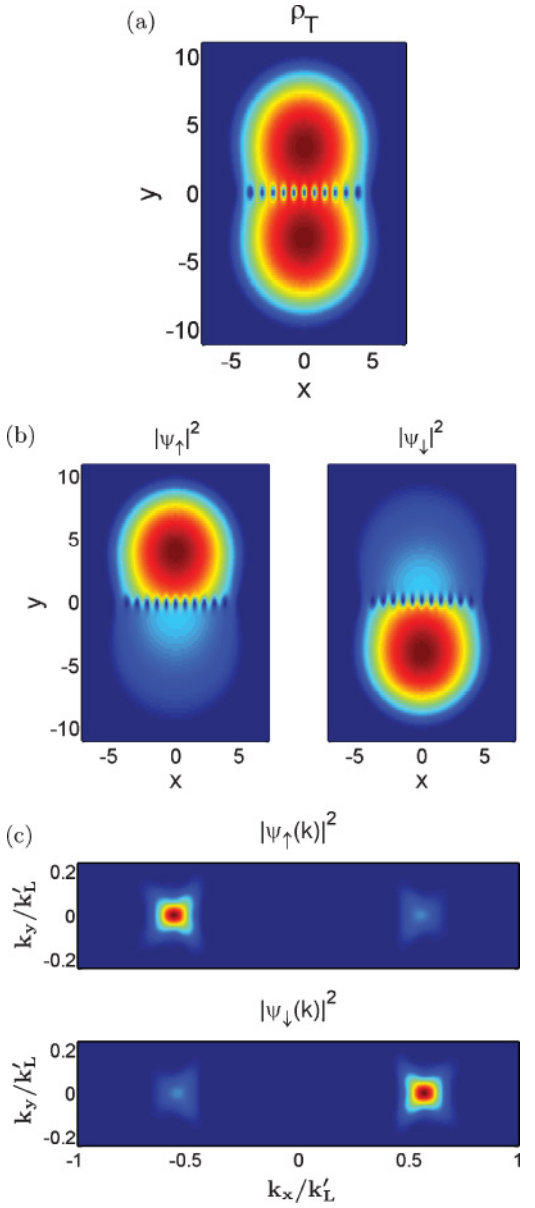

FIG. 7. (Color online) The figure shows results for $\Omega = 5E_L$, $\beta = 12\hbar\omega/a_0$, and $\gamma = 1$. (a) The total density is shown. The series of minima at $y = 0$ comes from vortices in the $|\uparrow\rangle$ and $|\downarrow\rangle$ wave functions (b). Momentum distribution of the $|\uparrow\rangle$ and $|\downarrow\rangle$ components is shown in (c).

for critical magnetic field of a single-component 2D gas in the Thomas-Fermi limit: $B_c = 4(a_0/R)^2 \ln[0.888(R/a_0)^2]$, where R is the Thomas-Fermi radius of the cloud [43]. We take $R = 6.5\,a_0$ (the size of our cloud), which gives $B_c \approx 0.35$. It is important to notice that larger number of particles or stronger interactions increase R, which lowers the critical field (B_c decreases with increasing R). To find B_c, we did simulations for $\Omega = 10E_L$, $\gamma = 1$, and for different values of β (which controls the strength of the effective magnetic field). We found that the vortices start to appear for a critical effective magnetic field $B_c \approx 0.34$, which is very close to our estimate presented above.

If the effective field is strong enough, a vortex "lattice" is formed, as shown in Fig. 11, which corresponds to $\Omega = 10E_L$,

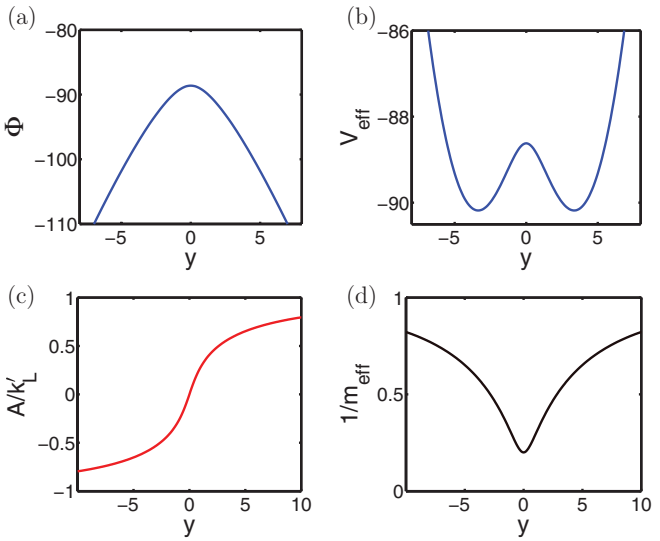

FIG. 8. (Color online) (a) The scalar potential $\Phi(y)$, (b) the effective trapping potential in $\hat{\mathbf{y}}$ direction $V_{\text{eff}}(y)$, (c) vector potential $A(y)$, and (d) inverse of the effective mass for $\Omega = 5E_L$, $\beta = 12\hbar\omega/a_0$, and $\gamma = 1$.

$\beta = 40\hbar\omega/a_0$, and $\gamma = 1.85$. From the figure, we see that vortices are concentrated along the x axis and around $y = 0$. This is because $B_{\text{eff}}(y)$ is not homogeneous, i.e., the field is strongest at $y = 0$ and it weakens with increasing $|y|$. We had to increase trapping strength in the $\hat{\mathbf{y}}$ direction ($\gamma = 1.85$) because the scalar potential $\Phi(y)$ separates the clouds [e.g., see Fig. 8(a)] and for a weaker trapping strength, the effective potential would have two minima [it would look like effective potential in Fig. 8(b)].

The most interesting regime is the one in which left and right moving phases $(\psi_{\uparrow L}(\mathbf{r}), \psi_{\downarrow L}(\mathbf{r}))$ and $(\psi_{\uparrow R}(\mathbf{r}), \psi_{\downarrow R}(\mathbf{r}))$

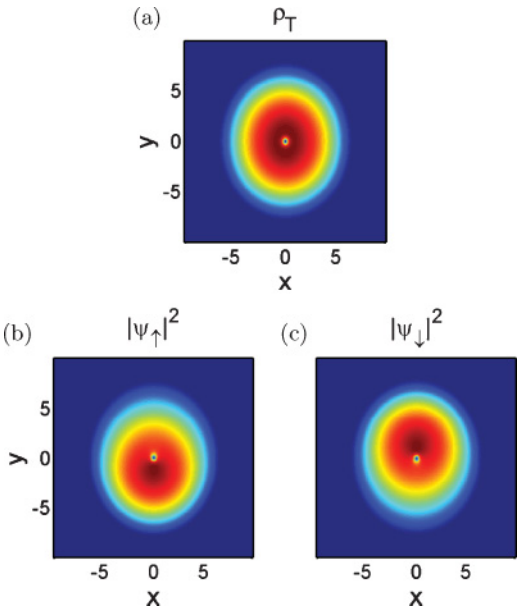

FIG. 9. (Color online) The figure shows results for $\Omega = 10E_L$, $\beta = 12\hbar\omega/a_0$, and $\gamma = 1$. In (a) the total density is shown, while (b) and (c) show densities of the $|\uparrow\rangle$ and $|\downarrow\rangle$ components. The vortex in the center appears for a strong-enough effective magnetic field.

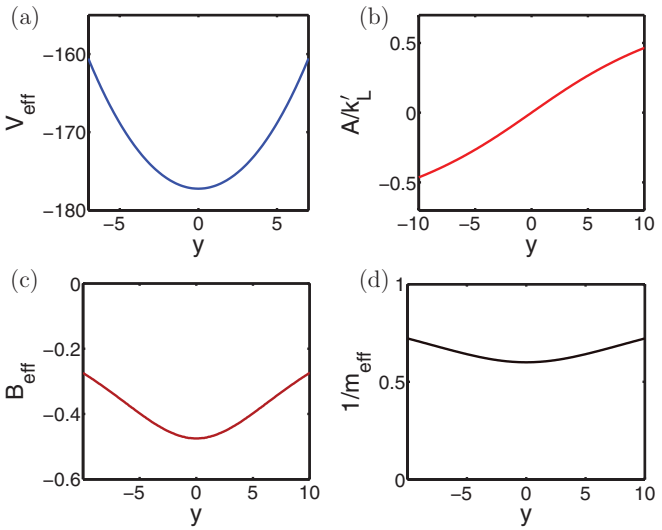

FIG. 10. (Color online) (a) The effective trapping potential in the $\hat{y}$ direction $V_{\text{eff}}(y)$, (b) the vector potential $A(y)$, (c) the effective magnetic field B_{eff}, and (d) the inverse of the effective mass for $\Omega = 10E_L$, $\beta = 12\hbar\omega/a_0$, and $\gamma = 1$.

are spatially separated along the $\hat{y}$ direction and there is a vortex (or vortices) in each phase in addition to a vortex line. This requires a double minimum structure of the effective potential in the $\hat{y}$ direction $V_{\text{eff}}(y)$, which separates the phases and strong enough effective magnetic field in each phase to create additional vortices, which tend to appear in pairs (i.e., the number of vortices is equal in both phases which is a consequence of the fact that in our simulations the effective gauge field is symmetric with respect to reflection about the $y = 0$ line and interactions are almost spin independent).

In Fig. 12(a), we show results for $\omega = 2\pi \times 10$ Hz, $\Omega = 4E_L$, $\beta = 20\hbar\omega/a_0$ [$a_0 = \sqrt{\hbar/(m\omega)}$]. By choosing $\omega = 2\pi \times 10$ Hz, parameter k'_L in dimensionless GP equations (22) becomes $k'_L = 18.83$, while interaction coefficients stay the same ($g_1 = 1600$, $g_2 = 1593$, and $g_{12} = 1593$). Having larger k'_L means we can create a stronger effective magnetic field. We increased the trapping frequency in the $\hat{y}$ direction ($\gamma = 1.3$) to bring two phases closer to $y = 0$, where the effective magnetic field is stronger [to counter the effective scalar potential $\Phi(y)$, which separates the phases]. In Fig. 12(b) we show results for

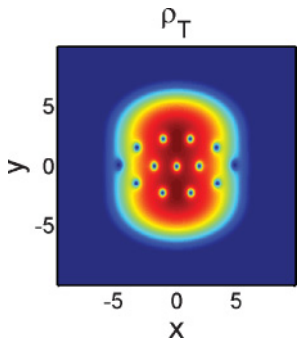

FIG. 11. (Color online) The total density for $\Omega = 10E_L$, $\beta = 40\hbar\omega/a_0$, and $\gamma = 1.85$.

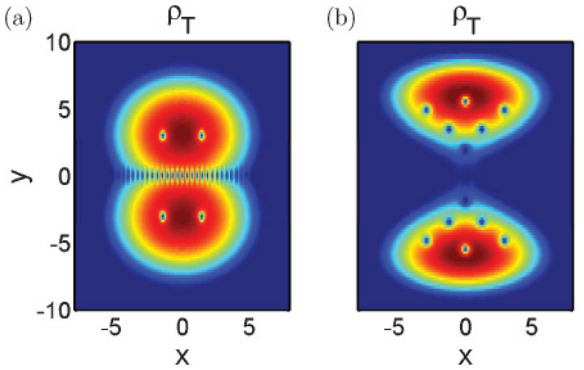

FIG. 12. (Color online) Figures show separated left and right phases with vortices in each phase. Trapping frequency is $\omega = 2\pi \times 10$ Hz. (a) Total density for $\Omega = 4E_L$, $\beta = 20\hbar\omega/a_0$, and $\gamma = 1.3$. (b) Total density for $\Omega = 10E_L$, $\beta = 150\hbar\omega/a_0$, and $\gamma = 2.75$.

$\omega = 2\pi \times 10$ Hz, $\Omega = 10E_L$, $\beta = 150\hbar\omega/a_0$, and $\gamma = 2.75$. Here the left and right phases are completely separated in space and the effective magnetic field is strong enough to produce multiple vortices in each phase. Also, it is clear that the vortices are not located in the centers of the two phases but are positioned closer to $y = 0$, which is expected because the field is stronger near $y = 0$.

It is important to discuss the means of experimentally observing results we presented. We concentrate on the time-of-flight imaging, which is widely used to probe cold-atoms systems. The time-of-flight picture here will be determined by the underlying momentum distribution of particles. If this momentum distribution consists of two separated peaks, the initial cloud will strongly separate during expansion (see, for example, Refs. [3,4]). We note that, due to the transformation $\psi'_\uparrow(\mathbf{r}) = \psi_\uparrow(\mathbf{r})e^{-ik_L x}$, $\psi'_\downarrow(\mathbf{r}) = \psi_\downarrow(\mathbf{r})e^{ik_L x}$ used when deriving Hamiltonian (21), the real momentum distribution of $|\uparrow\rangle$ particles will, in fact, be shifted by k_L with respect to the momentum distribution shown in figures and the momentum distribution of $|\downarrow\rangle$ particles is shifted by $-k_L$ (see Ref. [4]). In the case of $\Omega = 0$, both $|\uparrow\rangle$ and $|\downarrow\rangle$ particles will have zero average momentum, which means both components of the condensate will expand, while the position of the center of mass will be stationary during time of flight. For $\Omega = 3E_L$ and $\beta = 8\hbar\omega/a_0$, we expect four separated clouds to be seen in the time of flight: Since the real momentum distributions of the $|\uparrow\rangle$ and $|\downarrow\rangle$ particles are shifted by k_L and $-k_L$, there will be two clouds of $|\uparrow\rangle$ particles with average momenta of $0.2k_L$ (larger cloud) and $1.8k_L$ (smaller cloud) and two clouds of $|\downarrow\rangle$ particles with average momenta of $-0.2k_L$ (larger cloud) and $-1.8k_L$ (smaller cloud). It is important to notice that the vortex line will not be easily visible in those images, because it exists only due to the the overlap of the wave packets with different average momenta. During the time of flight, two wave packets $(\psi_{\uparrow L}, \psi_{\uparrow R})$ or $(\psi_{\downarrow L}, \psi_{\downarrow R})$ separate, which means that they no longer overlap and there is no clear vortex line present. For the case in Fig. 12, the vortices in each phase will be visible since they are not a result of overlapping the left- and right-moving condensates.

V. CONCLUSION

In this paper, we have investigated realistic experimental methods that can be used to create vortex excitations in spin-orbit-coupled Bose-Einstein condensates. The main conclusion of the work is that, due to a complicated interplay between effects associated with the applied laser fields and rotation, the resulting state of the spin-orbit BEC under additional perturbations is highly nonuniversal and depends strongly on the system parameters and specific laser schemes. In particular, we argued that a spin-orbit BEC under rotation of the trap alone does not achieve a thermodynamically stable state at all but acquires a complicated nonequilibrium dynamics that eventually leads to heating and the destruction of the condensate.

We have also suggested two alternative experimental methods to mimic an Abelian "orbital" magnetic field that involve either rotation of the entire experimental setup or a spatially dependent detuning. We performed numerical simulations of the resulting thermodynamically stable density distributions, focusing mostly on the M scheme that has already been realized experimentally. This scheme gives rise to an "Abelian" spin-orbit coupling with a well-understood ground state that we used as a basis of our numerical simulations that showed topological excitations above the ground state. We expect that the predicted vortex configurations, in particular, vortices appearing in pairs in the spatially separated left- and right-moving regions, would be straightforward to observe experimentally, as all necessary ingredients are already experimentally available.

Finally, we mention that to this point only an "Abelian" spin-orbit-coupling scheme has been actually realized in experiment [4] and we mostly focused here on vortex topological excitations in such systems with a well-understood ground state. What remains of great interest, of course, is an expermiental realization of a truly "non-Abelian" spin-orbit interaction (either of pure Rashba or Dresselhaus type or a nonequal mixture of those), which can be achieved using laser schemes described in Secs. IIB and IIC and Refs. [13,24]. Note that it was argued theoretically [14] that in the Rashba-Dresselhaus system with single-particle dispersion of the double-well type, a fragmented condensed state [44,45] can be selected by energetics for repulsive interactions that do not break the underlying Kramers symmetry. It arises because repulsive interactions in the real space tend to localize particles in the dual momentum space per the fundamental Heisenberg uncertainty principle. This robust argument together with the protection provided by Kramers symmetry and momentum conservation (modulo finite-size effects due to the trap) suggest that the long-sought-after fragmented BEC or, equivalently, a many-body Schrödinger's cat state is more stable in spin-orbit-coupled systems than in BECs in real-space double-well potentials and, hence, can be observed experimentally. Topological excitations above this exotic ground state are expected to be of an exotic nature and may potentially realize much of the exciting physics discussed in the context of two-component superconductors [46,47]. Finally, the nature of the ground state and topological excitations above it in the pure bosonic Rashba model remains of great interest as well. Depending on the interaction parameters, this model with a continuous ring of minima on a circle in momentum space, may potentially host topological BECs, a spontaneous symmetry-broken state [33], and exotic Bose-liquid states [48] where strong quantum fluctuations would prohibit order even at zero temperature.

Note added. Recently, we became aware of two papers that study spin-orbit-coupled BECs under rotation [49,50]. The fundamental assumptions in these papers qualitatively differ from our theory in that Refs. [49,50] start with an effective spin-orbit-coupled Hamiltonian and assume that it remains stationary under rotation. This is in contrast to our theory, where we consider realistic experimental schemes, where rotation is shown to lead to a different description.

ACKNOWLEDGMENTS

Authors are grateful to Austen Lamacraft, Egor Babaev, and Sankar Das Sarma for useful discussions. This work was supported by ARO via the atomtronics MURI (J. R. and I. B. S.) and DARPA's OLE program (I. B. S.) and a US-ARO grant, "Spin-orbit-coupled BECs " (T. A. S. and V. G.).

APPENDIX A: M SCHEME WITH ROTATING TRAP AND SPIN-ORBIT LASERS

The Hamiltonian in the rotating frame (6) is:

$$\hat{H}_{\mathrm{RF}} = \left[\frac{\hbar^2\hat{\mathbf{k}}^2}{2m} + V(\mathbf{r}) - \omega_r\hat{L}_z\right]\check{1} + \begin{pmatrix}\hbar(-\omega_z+\omega_q) & 0 & 0\\ 0 & 0 & 0\\ 0 & 0 & \hbar\omega_z\end{pmatrix} + \sqrt{2}\Omega\check{\sigma}_{3,x}\cos(2k_Lx + \Delta\omega_L t) - \omega_r\check{\sigma}_{3,z}. \quad \text{(A1)}$$

The Hamiltonian becomes time independent if we transfer to the rotating-wave frame and if we do the rotating-wave approximation:

$$\hat{H}_{\mathrm{RF}} = \left[\frac{\hbar^2\hat{\mathbf{k}}^2}{2m} + V(\mathbf{r}) - \omega_r\hat{L}_z\right]\check{1} + \begin{pmatrix}\delta+\hbar\omega_q & 0 & 0\\ 0 & 0 & 0\\ 0 & 0 & -\delta\end{pmatrix} + \frac{\Omega}{\sqrt{2}}\check{\sigma}_{3,x}\cos(2k_Lx) - \frac{\Omega}{\sqrt{2}}\check{\sigma}_{3,y}\sin(2k_Lx) - \hbar\omega_r\check{\sigma}_{3,z}, \quad \text{(A2)}$$

where $\delta = \hbar(\Delta\omega_L - \omega_z)$. We set quadratic Zeeman shift $\hbar\omega_q$ to be much greater than Ω and δ so we may restrict to the subspace spanned by $\{|m_z = 0\rangle, |m_z = -1\rangle\}$:

$$\hat{H}_{\mathrm{RF},2} = \left[\frac{\hbar^2\hat{\mathbf{k}}^2}{2m} + V(\mathbf{r}) - \omega_r\hat{L}_z\right]\check{1} + \frac{\Omega}{2}\check{\sigma}_x\cos(2k_Lx) - \frac{\Omega}{2}\check{\sigma}_y\sin(2k_Lx) + \begin{pmatrix}0 & 0\\ 0 & \hbar\omega_r-\delta\end{pmatrix}, \quad \text{(A3)}$$

where $\check{1}$ is 2×2 unit matrix and $\check{\sigma}_{x,y,z}$ are 2×2 Pauli matrices. Since there are effectively two internal degrees of freedom

we introduce pseudospin-1/2 notation, i.e., we define $|\uparrow\rangle \equiv |m_z = 0\rangle$, $|\downarrow\rangle \equiv |m_z = -1\rangle$. We follow the steps in Ref. [4] and make the following transformation: $\psi'_\uparrow(\mathbf{r}) = \psi_\uparrow(\mathbf{r})e^{-ik_L x}$, $\psi'_\downarrow(\mathbf{r}) = \psi_\downarrow(\mathbf{r})e^{ik_L x}$, where $(\psi_\uparrow(\mathbf{r}), \psi_\downarrow(\mathbf{r}))$ is a spinor wave function on which Hamiltonian (A3) acts. The Hamiltonian then becomes

$$\hat{H}_{\mathrm{RF},2} = \left[\frac{\hbar^2\hat{\mathbf{k}}^2}{2m} + V(\mathbf{r}) - \omega_r\hat{L}_z + E_L\right]\check{1} + \frac{\hbar^2 k_L\hat{k}_x}{m}\check{\sigma}_z + \frac{\Omega}{2}\check{\sigma}_x + \hbar\omega_r k_L y\check{\sigma}_z + \begin{pmatrix} 0 & 0 \\ 0 & \hbar\omega_r - \delta \end{pmatrix}, \quad \text{(A4)}$$

where $E_L = \hbar^2 k_L^2/2m$. We can drop the $E_L\check{1}$ term by simply renormalizing the energy.

APPENDIX B: M SCHEME WITH ROTATING TRAP

The Hamiltonian $\hat{H}'_{\mathrm{rot}}$ describing the M scheme with the rotating trap in the laboratory frame is

$$\hat{H}'_{\mathrm{rot}} = \left[\frac{\hbar^2\hat{\mathbf{k}}^2}{2m} + V(x(t), y(t), z) - \omega_r\hat{L}_z\right]\check{1} + \begin{pmatrix} \hbar(-\omega_z + \omega_q) & 0 & 0 \\ 0 & 0 & 0 \\ 0 & 0 & \hbar\omega_z \end{pmatrix} + \sqrt{2}\Omega\check{\sigma}_{3,x}\cos(2k_L x + \Delta\omega_L t), \quad \text{(B1)}$$

where $x(t)$ is defined in Eq. (3). After transferring to the rotating frame ($\hat{U}(t) = \exp[i\omega_r t(\hat{L}_z + \hat{S}_z)/\hbar]$) and making the rotating-wave approximation, the Hamiltonian is

$$\hat{H}'_{\mathrm{RF}} = \left[\frac{\hbar^2\hat{\mathbf{k}}^2}{2m} + V(\mathbf{r}) - \omega_r\hat{L}_z\right]\check{1} - \hbar\omega_r\check{\sigma}_{3,z} + \begin{pmatrix} 3\delta/2 + \hbar\omega_q & 0 & 0 \\ 0 & \delta/2 & 0 \\ 0 & 0 & -\delta/2 \end{pmatrix} + \frac{\Omega}{\sqrt{2}}\check{\sigma}_{3,x}\cos[2k_L x'(t) + \omega_r t] - \frac{\Omega}{\sqrt{2}}\check{\sigma}_{3,y}\sin[2k_L x'(t) + \omega_r t], \quad \text{(B2)}$$

where $x'(t) = x\cos(\omega_r t) - y\sin(\omega_r t)$. We may, again, neglect state $|m_z = 1\rangle$ assuming $\omega_q \gg$. To get the Hamiltonian in a more familiar spin-orbit-coupling form we make the following transformation: $\psi'_\uparrow(\mathbf{r}) = \psi_\uparrow(\mathbf{r})e^{-ik_L x'(t)}$, $\psi'_\downarrow(\mathbf{r}) = \psi_\downarrow(\mathbf{r})e^{ik_L x'(t) + i\omega_r t}$, which gives

$$\hat{H}'_{\mathrm{RF},2} = \left[\frac{\hbar^2\hat{\mathbf{k}}^2}{2m} + V(\mathbf{r}) - \omega_r\hat{L}_z + E_L\right]\check{1} + \frac{\hbar^2 k_L}{m}\hat{k}_x(t)\check{\sigma}_z + \frac{\Omega}{2}\check{\sigma}_x + \frac{\delta}{2}\check{\sigma}_z, \quad \text{(B3)}$$

where $\hat{k}_x(t) = \hat{k}_x\cos(\omega_r t) - \hat{k}_y\sin(\omega_r t)$. We can drop the $E_L\check{1}$ term by renormalizing the energy.

APPENDIX C: TRIPOD SCHEME WITH ROTATING TRAP AND SPIN-ORBIT LASERS

The original Hamiltonian for the tripod scheme (stationary system) is (see Ref. [13]):

$$\hat{H}_0 = \frac{\hat{\mathbf{p}}^2}{2m}\check{1} + \hat{V}(\mathbf{r}) + \hat{H}_{a-l}, \quad \text{(C1)}$$

where $\hat{V}(\mathbf{r}) = \sum_j V_j(\mathbf{r})|j\rangle\langle j|$ is the spin-dependent trapping potential, the atom-laser interaction $\hat{H}_{a-l} = \Delta|0\rangle\langle 0| - (\Omega_1|0\rangle\langle 1| + \Omega_2|0\rangle\langle 2| + \Omega_3|0\rangle\langle 3| + \mathrm{H.c.})$, and $\check{1}$ is the 4×4 unit matrix. Additionally, Δ is the detuning from resonance and $\Omega_{1,2,3}$ are Rabi frequencies, $\Omega_1(\mathbf{r}) = \Omega\sin\theta\cos(mv_a x)e^{imv_b y}$, $\Omega_2(\mathbf{r}) = \Omega\sin\theta\sin(mv_a x)e^{imv_b y}$, and $\Omega_1(\mathbf{r}) = \Omega\cos\theta$, where Ω, θ, v_a, and v_b are constants (see Refs. [13,14] for details). If we start rotating spin-orbit lasers in the laboratory, the atom-laser interaction part of the Hamiltonian becomes $e^{-i\omega_r t(\hat{L}_z+\hat{S}_z)/\hbar}\hat{H}_{a-l}e^{i\omega_r t(\hat{L}_z+\hat{S}_z)/\hbar}$. If the trap rotates, the trapping potential becomes $e^{-i\omega_r t(\hat{L}_z+\hat{S}_z)/\hbar}\hat{V}e^{i\omega_r t(\hat{L}_z+\hat{S}_z)/\hbar}$. Therefore, we can write the Hamiltonian of the rotating system as

$$\hat{H}_{\mathrm{rot}} = e^{-i\omega_r t(\hat{L}_z+\hat{S}_z)/\hbar}\hat{H}_0 e^{i\omega_r t(\hat{L}_z+\hat{S}_z)/\hbar}. \quad \text{(C2)}$$

The Hamiltonian in the rotating frame is then $\hat{H}_{\mathrm{RF}} = \hat{H}_0 - \omega_r(\hat{L}_z + \hat{S}_z)$. Since $\hat{H}_{\mathrm{RF}}$ is time independent we can use exactly the same procedure for getting the effective spin-orbit coupling described in Refs. [8,13], i.e. we project the Hamiltonian to the dark states subspace. Here we assume that three degenerate hyperfine ground states are part of the $F = 1$ manifold (for example, the ground state of ^{87}Rb) and that they are eigenstates of $\hat{S}_z$. This gives us the precise form of $\hat{S}_z$ operator. As in Ref. [13] we take $V_1 = V_2 = w(\mathbf{r})$ and $V_3 = w(\mathbf{r}) + \delta$. After projecting to the dark states we get:

$$\hat{H}_{\mathrm{RF},2} = \left[\frac{\hat{\mathbf{p}}^2}{2m} + w(\mathbf{r}) - \omega_r\hat{L}_z\right]\check{1} - v_0\hat{p}_x\check{\sigma}_y - v_1\hat{p}_y\check{\sigma}_z + \delta_0\check{\sigma}_z + m\hbar\omega_r(v_1 x\check{\sigma}_z - v_0 y\check{\sigma}_y) - \hbar\omega_r\begin{pmatrix} \sin^2\phi & \sin\phi\cos\phi\cos\theta \\ \sin\phi\cos\phi\cos\theta & \cos^2\theta\cos^2\phi - \sin^2\theta \end{pmatrix}, \quad \text{(C3)}$$

where $\phi = mv_0 x/\cos\theta$ and $\delta_0 = \sin^2\theta\{\delta - [(\frac{v_0}{\cos\theta})^2 + (\frac{v_1}{\sin^2(\theta/2)})^2]/2\}/2$.

[1] I. Zutić, J. Fabian, and S. D. Sarma, Rev. Mod. Phys. **76**, 323 (2004).

[2] Y.-J. Lin, R. L. Compton, A. R. Perry, W. D. Phillips, J. V. Porto, and I. B. Spielman, Phys. Rev. Lett. **102**, 130401 (2009).

[3] Y.-J. Lin, R. L. Compton, K. Jimenez-Garcia, J. V. Porto, and I. B. Spielman, Nature **462**, 628 (2009).
[4] Y.-J. Lin, K. Jimenez-Garcia, and I. B. Spielman, Nature **471**, 83 (2011).
[5] Y.-J. Lin, R. L. Compton, K. Jimenez-Garcia, W. D. Phillips, J. V. Porto, and I. B. Spielman, Nat. Phys. **7**, 531 (2011).
[6] G. Juzeliūnas and P. Öhberg, Phys. Rev. Lett. **93**, 033602 (2004).
[7] G. Juzeliūnas, P. Öhberg, J. Ruseckas, and A. Klein, Phys. Rev. A **71**, 053614 (2005).
[8] J. Ruseckas, G. Juzeliūnas, P. Öhberg, and M. Fleischhauer, Phys. Rev. Lett. **95**, 010404 (2005).
[9] D. Jaksch and P. Zoller, New. J. Phys. **5**, 56 (2003).
[10] K. Osterloh, M. Baig, L. Santos, P. Zoller, and M. Lewenstein, Phys. Rev. Lett. **95**, 010403 (2005).
[11] S. S. Zhu, H. Fu, C. J. Wu, S. C. Zhang, and L. M. Duan, Phys. Rev. Lett. **97**, 240401 (2006).
[12] I. I. Satija, D. C. Dakin, and C. W. Clark, Phys. Rev. Lett. **97**, 216401 (2006).
[13] T. D. Stanescu, C. Zhang, and V. M. Galitski, Phys. Rev. Lett. **99**, 110403 (2007).
[14] T. D. Stanescu, B. Anderson, and V. Galitski, Phys. Rev. A **78**, 023616 (2008).
[15] J. D. Koralek, C. P. Weber, J. Orenstein, B. A. Bernevig, S.-C. Zhang, S. Mack, and D. Awschalom, Nature **458**, 610 (2009).
[16] T. D. Stanescu and V. Galitski, Phys. Rev. B **75**, 125307 (2007).
[17] M. Z. Hasan and C. L. Kane, Rev. Mod. Phys. **82**, 3045 (2010).
[18] J. Schliemann, J. C. Egues, and D. Loss, Phys. Rev. Lett. **90**, 146801 (2003).
[19] O. Chalaev and D. Loss, Phys. Rev. B **71**, 245318 (2005).
[20] B. A. Bernevig, J. Orenstein, and S.-C. Zhang, Phys. Rev. Lett. **97**, 236601 (2006).
[21] J. Schliemann, J. C. Egues, and D. Loss, Phys. Rev. B **80**, 235327 (2009).
[22] T.-L. Ho and S. Zhang, Phys. Rev. Lett. **107**, 150403 (2011).
[23] G. Juzeliūnas, J. Ruseckas, and J. Dalibard, Phys. Rev. A **81**, 053403 (2010).
[24] D. L. Campbell, G. Juzeliūnas, and I. B. Spielman, Phys. Rev. A **84**, 025602 (2011).
[25] J. Larson and E. Sjoqvist, Phys. Rev. A **79**, 043627 (2009).
[26] C. Wang, C. Gao, C.-M. Jian, and H. Zhai, Phys. Rev. Lett. **105**, 160403 (2010).
[27] S.-K. Yip, Phys. Rev. A **83**, 043616 (2011).
[28] Y. Zhang, L. Mao, and C. Zhang, e-print arXiv:1102.4045 (2011).
[29] Z. F. Xu, R. Lu, and L. You, Phys. Rev. A **83**, 053602 (2011).
[30] T. Kawakami, T. Mizushima, and K. Machida, Phys. Rev. A **84**, 011607(R) (2011).
[31] C.-M. Jian and H. Zhai, Phys. Rev. B **84**, 060508(R) (2011).
[32] D.-W. Zhang, Z.-Y. Xue, H. Yan, Z. D. Wang, and S.-L. Zhu, e-print arXiv:1104.0444 (2011).
[33] S. Gopalakrishnan, A. Lamacraft, and P. M. Goldbart, e-print arXiv:1106.2552 (2011).
[34] C. Wu, I. Mondragon-Shem, and X.-F. Zhou, Chinese Phys. Lett. **28**, 097102 (2011).
[35] J. Dalibard, F. Gerbier, G. Juzeliūnas, and P. Öhberg, e-print arXiv:1008.5378 (2010).
[36] A. J. Leggett, Rev. Mod. Phys. **73**, 307 (2001).
[37] A. J. Leggett, in *Bose-Einstein Condensation: From Atomic Physics to Quantum Fluids*, Proceedings of the 13th Physics Summer School, edited by C. M. Savage and M. Das (World Scientific, Singapore, 2000).
[38] Y. Castin and R. Dum, Eur. Phys. J. D **7**, 399 (1999).
[39] M. Burrello and A. Trombettoni, Phys. Rev. Lett. **105**, 125304 (2010).
[40] F. Dalfovo and S. Stringari, Phys. Rev. A **53**, 2477 (1996).
[41] K. Kasamatsu, M. Tsubota, and M. Ueda, Phys. Rev. Lett. **91**, 150406 (2003).
[42] I. B. Spielman, Phys. Rev. A **79**, 063613 (2009).
[43] The equation can be derived using expressions given in C. J. Pethick and H. Smith, *Bose-Einstein Condensation in Dilute Gases* (Cambridge University Press, Cambridge, England, 2008).
[44] A. Ashhab and A. J. Leggett, Phys. Rev. A **68**, 063612 (2003).
[45] E. J. Mueller, T.-L. Ho, M. Ueda, and G. Baym, Phys. Rev. A **74**, 033612 (2006).
[46] E. Babaev, A. Sudbo, and N. W. Aschroft, Nature **431**, 666 (2004).
[47] E. Babaev and N. W. Aschroft, Nat. Phys. **3**, 530 (2007).
[48] C. N. Varney, K. Sun, V. Galitski, and M. Rigol, Phys. Rev. Lett. **107**, 077201 (2011).
[49] X. Q. Xu and J. H. Han, Phys. Rev. Lett. **107**, 200401 (2011).
[50] X.-F. Zhou, J. Zhou, and C. Wu, e-print arXiv:1108.1238 (2011).